PHYSICAL REVIEW E **76**, 021501 (2007)

Statistical and sampling issues when using multiple particle tracking

Thierry Savin and Patrick S. Doyle*
Chemical Engineering Department, Massachusetts Institute of Technology, 77 Massachusetts Avenue, Cambridge, Massachusetts 02139, USA

(Received 14 December 2006; published 8 August 2007)

Video microscopy can be used to simultaneously track several microparticles embedded in a complex material. The trajectories are used to extract a sample of displacements at random locations in the material. From this sample, averaged quantities characterizing the dynamics of the probes are calculated to evaluate structural and/or mechanical properties of the assessed material. However, the sampling of measured displacements in heterogeneous systems is singular because the volume of observation with video microscopy is finite. By carefully characterizing the sampling design in the experimental output of the multiple particle tracking technique, we derive estimators for the mean and variance of the probes' dynamics that are independent of the peculiar statistical characteristics. We expose stringent tests of these estimators using simulated and experimental complex systems with a known heterogeneous structure. Up to a certain fundamental limitation, which we characterize through a material degree of sampling by the embedded probe tracking, these estimators can be applied to quantify the heterogeneity of a material, providing an original and intelligible kind of information on complex fluid properties. More generally, we show that the precise assessment of the statistics in the multiple particle tracking output sample of observations is essential in order to provide accurate unbiased measurements.

DOI: 10.1103/PhysRevE.76.021501 PACS number(s): 83.10.Pp, 05.40.−a, 07.05.Kf, 83.80.Kn

INTRODUCTION

Soft matter scientists have expressed an increasing interest in resolving the structure of complex fluids at a micron-size length scale. This interest is justified by the implication of the spatial micro-organization of the components of a complex material in its transport, rheological, and optical properties at equilibrium (see Ref. [1] and references therein), as well as in its eventual kinetics of formation [2,3]. This microscale characterization has also been shown to be particularly important in biological applications. From inter- and intracellular transport phenomena to molecular motor activity, the driving (or resisting) forces occur on micron and submicron length scales, and cannot be inferred from bulk measurements [4,5]. Also, in the biology framework, it has been reported that the fate and behavior of single cells depend on their local level of confinement [6] or the stiffness of their microenvironment [7]. More strikingly, it has been recently pointed out that, in general, systems with heterogeneous features can lead to apparently peculiar measurements, themselves leading to incorrect interpretations [8]. Thus, access to some measure of the spatial distribution of a given material property (pore size, viscoelasticity, charge density, etc.) provides fundamental information for the understanding of a plethora of phenomena involved in complex fluid science.

Consequently, the range of techniques available to achieve these goals has been broadened over recent decades. Direct observations of the structural elements and their organization are made possible thanks to a wide range of microscopy techniques. Light, fluorescence, electron, and atomic force microscopy are able to report a spatial mapping of the complex fluid structure at various length scales. Microscopy techniques provide us with two-dimensional pictures, and high-order measurements of the spatial distribution of structures can eventually be made from the micrographs by using image postprocessing techniques [9,10]. Three-dimensional information can be obtained from modified versions of the previous techniques (confocal and differential interference contrast for optical microscopy, quick-freeze deep-etch sample preparation for electron microscopy, etc.). Scattering techniques such as neutron, x-ray, and light scattering, however, spatially average the structural features in the sample and thus lose some information on the eventual heterogeneity.

Rheology of a complex fluid is intimately related to its network microstructure [11]. Compared to the morphological measurements described above, inferring structural information from rheological data is, however, a complicated inverse problem (see, for example, [12] for an application of rheometry to extract information on network heterogeneity). Direct microrheological mapping of a material is possible by scanning its surface with an atomic force microscope (see Ref. [13] and references therein), and has been addressed recently using a passive microrheology technique [14,15]. Passive microrheology measures the response of a material to the thermal motions of micron-sized probes. Under certain conditions, it reports either the local mechanical properties or the microstructure of the material in which the probes are embedded. Video multiple particle tracking is a simple and inexpensive microrheology technique that, to date, provides the highest throughput of spatial microrheological sampling of a material. It is a passive technique, where the thermal fluctuations of about a hundred particles dispersed in the material can be tracked simultaneously (see Ref. [16] for a detailed description of the technique). Measurements are usually fast, and the statistical errors are typically considered

---

*Author to whom correspondence should be addressed. Email address: pdoyle@mit.edu small because of the large amount of data collected. Its simplicity and availability have made it very popular, and in the last few years, investigation of microenvironments using video multiple particle tracking has been performed on various materials, such as actin systems, agarose gels, cells, and DNA solutions [17–20]. In recent studies, it has been used to extract the pore size distribution in cross-linked actin networks [21] and to characterize anisotropic gels of aligned DNA [22]. We also recall at this point that the material heterogeneity can be a problem for microrheologists trying to calculate bulk properties [23]. A method called two-point microrheology that tentatively overcomes this problem has recently been introduced using the cross correlation of the paired motions of the probes [24,25]. However, local one-point microrheology from video multiple particle tracking, as used in this paper, remains the only available method that can assess heterogeneity of a sample.

In this regard, the complex materials investigated with microrheology are often known to be heterogeneous, such that, depending on where the probe is located in the sample, its motion will exhibit different dynamics [26]. In parallel, due to the finite imaging volume, the amount of data collected from a given particle is limited by the duration of its residence in the volume of observation. The complexity comes from the fact that the duration of the measured particle trajectory depends also on the local material properties. For example, a model heterogeneous system can let some particles travel throughout its porous structure, but will tightly trap a subpopulation of particles in its smaller pores (such dynamically bimodal behavior has been observed in actin gels [27]). The trapped particles will be tracked for the whole acquisition time, whereas free particles will leave the volume of observation and/or enter—possibly several times—during the same acquisition time. As a result, numerous short trajectories will be extracted in regions of loose meshing where particles are free to move, whereas only a few long trajectories will be extracted from the signal of trapped particles, even if the material hypothetically exhibits the same amount of small and large pores. This toy model example gives an immediate sense of the peculiar statistical sampling of a heterogeneous material using this technique. The sampling depends on both the size of the imaging volume and the probed material's structure.

Ultimately, the distribution of material properties needs to be characterized independently of the measurement technique. The distribution of a given property can be quantified by its mean, variance, skewness, kurtosis, and other higher-order moments or functions of moments, such as the non-Gaussian parameters [28]. The latter have already been used to quantify dynamical heterogeneity in colloidal systems [29,30]. Through the dynamics of the probes, the material heterogeneity is indirectly, but almost uniquely, quantified (see subsequent sections). For example, the mean of the probes' individual mean-squared displacements, that is, the ensemble-averaged mean-squared displacement, is usually calculated by dividing in time individual trajectories into displacements and accounting for all displacements in the same way, disregarding the trajectory they were extracted from (a simultaneous time and ensemble average is thus performed). But the ensemble-averaged mean-squared displacement has also been calculated as the center of the individual mean-squared displacement distribution obtained from prior time-averaging calculations on the individual trajectories [31]. Similar calculations based on time-averaged estimations from each probes' trajectory were used in Refs. [14,32] to perform qualitative analyses that circumvent, to a certain extent, the statistical limitations described in the previous paragraph.

In the current literature, we found only two methods to assess a material's heterogeneity using multiple particle tracking. In the first kind of heterogeneity study, bin partition analysis based on percentile calculations is used to improve statistical accuracy. This analysis was successful in assessing a number of mechanical mechanisms in the cellular machinery [2,3,19,20,33]. Nevertheless, it remains overall a qualitative perspective, since it compares results in complex systems with measurements in homogeneous glycerol solutions. It has, however, the advantage of being able to provide a somewhat surveyable degree of heterogeneity, allowing, for instance, the ordering of materials from the most heterogeneous to the least. In a second attempt, hypothesis testing based on the F ratio of paired mean-squared displacements was performed to classify particles' dynamics into statistically distinguishable groups [15]. Although it is not the more convenient way to quantify the heterogeneity (i.e., with a single number), this classification allowed the authors to map the locations of given microenvironments in an agarose gel sample. Following this idea, it is actually possible to test homogeneity of multiple dynamics at once using a single statistical test (see [34] for a review of available statistical methods).

In this paper, we develop a way to rigorously calculate the first two moments of the probe particle dynamics in a heterogeneous system. Using a mathematical formulation for the peculiar statistical sampling obtained from multiple particle tracking output, we derive estimators of these two moments (mean and variance) that are independent of the sampling design, up to a certain fundamental limitation of the technique that we call the material's detectability. In the first part, the theoretical approach is discussed and we introduce an important factor, called the degree of sampling, that quantifies the level of detectability of certain probe dynamics by the technique. From this approach, estimators for the two first moments of individual mean-squared displacements are derived. Section III provides stringent testing of these estimators on simulated and experimental systems of increasing complexity that cover a wide range of actual scenarios.

I. THEORY

A. Sampling design of multiple particle tracking

Let $\nu(\omega,\mathbf{x})$ be the value of a material property ν at the location $\mathbf{x}=(x,y,z)\in V$ in the material, evaluated at the frequency ω. We write as $P_{\nu(\omega)}(v)=V^{-1}\int_V\delta[v-\nu(\omega,\boldsymbol{\chi})]d\boldsymbol{\chi}$ the probability density function of this material property in a volume V of medium, where δ designates the Dirac delta function. A schematic of such a heterogeneous fluid is pictured in Fig. 1. An indicator of heterogeneity of the material in this volume is then given by the moments about the mean $\mathbb{E}[\nu(\omega)]$ of $P_{\nu(\omega)}:\mu_r[\nu(\omega)]=\mathbb{E}[\{\nu(\omega)-\mathbb{E}[\nu(\omega)]\}^r]$, where $\mathbb{E}[\cdots]$ designates the expectation value.

In a passive microrheology experiment such as the multiple particle tracking technique used in this paper, a measure of the local material property is made through the thermal motion of a micron-sized particle embedded in the material. A thermally fluctuating particle following the trajectory $\mathbf{x}(t)$ exhibits dynamics that, at a time scale $\tau=\omega^{-1}$, can be quantified by the distribution of the displacement $\mathbf{d}_t(\tau)=\mathbf{x}(t+\tau)-\mathbf{x}(t)$, given the position $\mathbf{x}(t)$ from which the step displacement is taken. Usually, a measure of the local material property is made by calculating the mean-squared displacement $m_t(\tau,\boldsymbol{\chi})=\mathbb{E}[\mathbf{d}_t(\tau)^2|\mathbf{x}(t)=\boldsymbol{\chi}]=\int\boldsymbol{\delta}^2P_{\mathbf{d}_t(\tau)|\mathbf{x}(t)}(\boldsymbol{\delta}|\boldsymbol{\chi})d\boldsymbol{\delta}$, where the integral runs over all possible displacements. This material property is defined at a location $\mathbf{x}(t)$, within a minimum length scale given by the extent $\mathbf{d}_t(\tau)$ of the trajectory (i.e., the amplitude of the deformation applied to the material), and over which the material is assumed homogeneous. From the stationary assumption, this property is independent of t, and we will write it $m(\tau,\boldsymbol{\chi})$. Hence the distribution that is accessible with the technique is $P_{m(\tau)|\mathbf{x}}(m|\boldsymbol{\chi})=\delta[m-m(\tau,\boldsymbol{\chi})]$ and the central moments (or moments about the mean) of $P^{\mathrm{u}}_{m(\tau)}(m)=V^{-1}\int_V P_{m(\tau)|\mathbf{x}}(m|\boldsymbol{\chi})d\boldsymbol{\chi}$, obtained with uniform spatial distribution of positions in the volume V $[P_{\mathbf{x}}(\boldsymbol{\chi})=V^{-1}]$, can be used to quantify the heterogeneity of the material through the probes' heterogeneous dynamics (we will expose some limitations to this idea in the next sections). Such moments can be written in terms of the raw moments,

$$\mathbb{E}[m(\tau)^r]=\int_0^{+\infty}m^rP^{\mathrm{u}}_{m(\tau)}(m)dm$$
$$=V^{-1}\int_V\left(\int\boldsymbol{\delta}^2P_{\mathbf{d}(\tau)|\mathbf{x}}(\boldsymbol{\delta}|\boldsymbol{\chi})d\boldsymbol{\delta}\right)^r d\boldsymbol{\chi}. \qquad (1)$$

We note at this point that, since the quantity to estimate involves two integrations, there will be two levels of sampling when performing the experiments. A first level of sampling is obtained in the spatial integration [outer integral in Eq. (1)] since, in practice, only a finite number of locations will be investigated. A second level of sampling needs to be characterized, as the number of sample displacements obtained per given sample location will be eventually small, and will thus require a binning of the volume of observation. It is then possible to gather observed displacements by grouping their corresponding locations into spatial bins, and then calculate the inner integral of Eq. (1) in each bin.

In the multiple particle tracking technique, trajectories of the probes' Brownian motion are obtained by processing movies acquired with video microscopy. The sampling of the material is limited in space by the volume of observation $V_{\mathrm{b}}\subset V$ (the camera field of view in the plane and the tracking depth in the direction perpendicular to the plane) which contains $N_{\mathrm{b}}(t)$ probe particles at a given time t (see Fig. 1). A limitation in time is naturally given by the duration of acquisition $T_{\mathrm{b}}=n_{\mathrm{b}}\Delta t$, where Δt is the time interval between two successive movie frames, and $n_{\mathrm{b}}+1$ is the number of frames. The output of the tracking is a set of N probe trajectories $\{\mathbf{x}_i(t)\}_{1\leqslant i\leqslant N}$, each trajectory being sampled every Δt. We will write as $\mathbf{X}=\{\{\mathbf{x}_{i,j}=\mathbf{x}_i(j\Delta t+t_i)\in V_{\mathrm{b}}\}_{0\leqslant j\leqslant n_i}\}_{1\leqslant i\leqslant N}$ the sample of observed positions, where $T_i=n_i\Delta t$ is the duration of the trajectory i, and t_i is the time of first observation. Several trajectories can eventually correspond to a single particle that leaves and comes back in the volume of observation, such that in general $N_{\mathrm{b}}(t)\leqslant N$ and $T_i\leqslant T_{\mathrm{b}}$. For a lag time $\tau=n\Delta t$ and for trajectories such that $T_i\geqslant\tau$ (i.e., $n_i\geqslant n$), we can extract $q_i(n)=n_i+1-n$ overlapping (hence *a priori* nonindependent; see the next section) displacements from the trajectory i, and we obtain the sample $\mathbf{D}(n)=\{\{\mathbf{d}_{i,j}(n)=\mathbf{x}_{i,j+n-1}-\mathbf{x}_{i,j-1}\}_{1\leqslant j\leqslant q_i(n)}\}_{i\in I(n)}$ of observed displacements, where $I(n)=\{i:n_i\geqslant n\}$ is the set of indices corresponding to trajectories longer than τ. The corresponding set of positions associated with $\mathbf{D}(n)$ will be written $\mathbf{X}(n)=\{\{\mathbf{x}_{i,j-1}\}_{1\leqslant j\leqslant q_i(n)}\}_{i\in I(n)}$ [45].

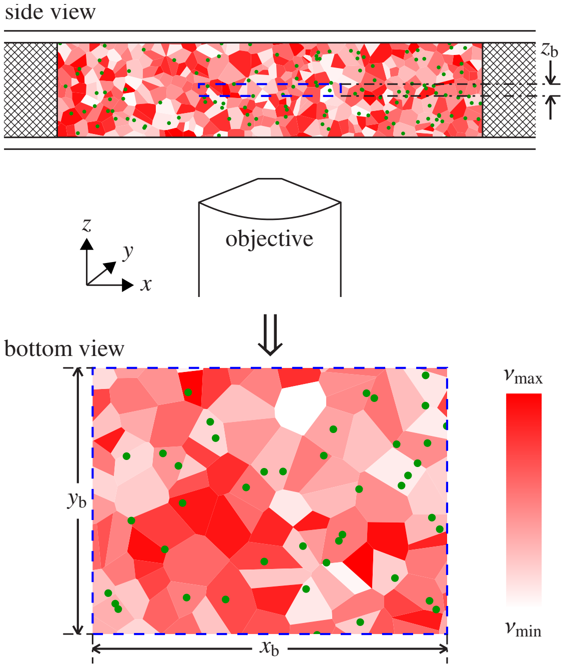

FIG. 1. (Color online) Schematic of a heterogeneous system as seen through a microscope. Different colors in the material correspond to different values of a certain material property ν. The material is held in a chamber of observation (side view) and randomly dispersed particles (represented by the dots) are visible only when moving in a certain imaging volume $V_{\mathrm{b}}=x_{\mathrm{b}}\times y_{\mathrm{b}}\times z_{\mathrm{b}}$ (dashed frame) whose smallest dimension z_{b} in the z direction determines the limitations in sampling. The bottom view pictures a typical snapshot at a given time t.

As noted earlier, in order to estimate Eq. (1) the volume V_{b} must be subdivided into M cells (or bins) of volume $\{V_k\}_{1\leqslant k\leqslant M}$, with $V_{\mathrm{b}}=\Sigma_{k=1}^{M}V_k$. To each bin corresponds a constant (assuming homogeneity on the bin size scale) value of the inner integral, which we will call $m_k(\tau)=\mathbb{E}[m(\tau,\boldsymbol{\chi})|\boldsymbol{\chi}\in V_k]=m(\tau,\boldsymbol{\chi}_k)$, where $\boldsymbol{\chi}_k\in V_k$ is a hypothetical location of V_k. Suppose that it is possible to determine $m_k(\tau)$ using an estimator with arbitrary certainty, $\hat{g}(\mathbf{D}_k^{\mathrm{v}}(n))$, such that

$\mathbb{E}[\hat{g}(\mathbf{D}_k^{\mathrm{v}}(n))]=m_k(\tau)$ from any subset $\mathbf{D}_k^{\mathrm{v}}(n)$ of $\mathbf{D}(n)$ containing only displacements $\{\mathbf{d}_{i,j}(n)\}$ for which the corresponding positions $\{\mathbf{x}_{i,j-1}\}$ are in V_k. By making such an assumption, we aim at characterizing the first level of sampling only, discarding the second level, which will be discussed later in the text. The estimators of the spatial moments of $m(\tau)$ are then

$$\hat{\mathbb{E}}[m(\tau)]=\sum_{k=1}^{M}\pi_k\hat{g}(\mathbf{D}_k^{\mathrm{v}}(n)),$$

$$\hat{\mu}_2[m(\tau)]=\frac{\sum_{k=1}^{M}\pi_k\left[\hat{g}(\mathbf{D}_k^{\mathrm{v}}(n))-\sum_{k=1}^{M}\pi_k\hat{g}(\mathbf{D}_k^{\mathrm{v}}(n))\right]^2}{\sum_{k=1}^{M}\pi_k(1-\pi_k)},\qquad(2)$$

where $\pi_k=V_k/V_{\mathrm{b}}$, as obtained from the usual sample estimators of the weighted mean and variance with uncorrelated samples [35]. The difficulty is to build the set $\{V_k\}_{1\leqslant k\leqslant M}$ such that, on the one hand the statistical accuracy within each cell is high enough (obtained by increasing V_k, which in turn will decrease M); on the other hand, the number of bins is large enough such that moments are accurately estimated and such that the assumption of uniformity within each cluster is valid by sampling the space at a fine enough scale (large M). In other words, there is a compromise between gaining accuracy in estimating the inner integral in Eq. (1) and accuracy in the outer integral calculation. For generality, it is convenient to have a formula independent of the choice of $\{V_k\}_{1\leqslant k\leqslant M}$. This can be achieved under some reasonable assumptions. We first assume that each trajectory is entirely contained in one of the bins $\{V_k\}_{1\leqslant k\leqslant M}$. We can then write

$$\hat{g}(\mathbf{D}_k^{\mathrm{v}}(n))=\left(\sum_{i\in I_k}n_i\right)^{-1}\sum_{i\in I_k}n_i\hat{g}(\mathbf{D}_i(n)),$$

where $\mathbf{D}_i(n)$ is the subset of $\mathbf{D}(n)$ corresponding to trajectory i, and I_k is the set of indices corresponding to trajectories contained in V_k. Next we assume that $(\Sigma_{i\in I_k}n_i)/V_k=C_{\mathrm{b}}n_{\mathrm{b}}$ is independent of k, where C_{b} is the uniform density of particle in the material (recall that $\Sigma_{i\in I_k}n_i$ is the total number of observed positions in V_k). We get

$$\hat{\mathbb{E}}[m(\tau)]=\sum_{i=1}^{N}p_i\hat{g}(\mathbf{D}_i(n)),$$

$$\hat{\mu}_2[m(\tau)]=\frac{\sum_{i=1}^{N}p_i\left[\hat{g}(\mathbf{D}_i(n))-\sum_{i=1}^{N}p_i\hat{g}(\mathbf{D}_i(n))\right]^2}{\sum_{k=1}^{M}\pi_k(1-\pi_k)},\qquad(3)$$

where $p_i=n_i/\Sigma_{i=1}^{N}n_i$. The denominator of $\hat{\mu}_2[m(\tau)]$ is a correcting factor for the bias, and approaches 1 for $M\gg 1$. As mentioned earlier, the use of Eq. (3) for the sample variance assumes that the probes' motions are mutually independent (or at least, uncorrelated). This is an acceptable approximation, since the residual correlation, measured for example in two-point microrheology techniques, is a higher-order hydrodynamic effect that vanishes with increasing interparticle distance. At this point, it is also possible to characterize the uncertainty of these estimators solely due to the first level of finite spatial sampling. Using again a common formula for the variance of the sample mean and of the sample variance [35], we have

$$\mu_2[\hat{\mathbb{E}}[m(\tau)]]=\mu_2[m(\tau)]\sum_{k=1}^{M}\pi_k^2,$$

$$\mu_2[\hat{\mu}_2[m(\tau)]]=\{\mu_4[m(\tau)]-\mu_2[m(\tau)]^2\}\sum_{k=1}^{M}\pi_k^2+O\left(\sum_{k=1}^{M}\pi_k^2\right).\qquad(4)$$

The calculation of the quantity $\Sigma_{k=1}^{M}\pi_k^2$ requires knowledge of the individual volumes V_k for all $1\leqslant k\leqslant M$. However, at an instant t of the measurement, the number of sample locations observed in the volume V_{b} is $N_{\mathrm{b}}(t)$. We can then argue for this calculation that the uncertainty in the first level of spatial sampling is proportional to $\mathbb{E}[N_{\mathrm{b}}(t)]^{-1}=N_{\mathrm{b}}^{-1}$. Thus we will write $\Sigma_{k=1}^{M}\pi_k^2\approx N_{\mathrm{b}}^{-1}$ when estimating the above quantities.

As pointed out earlier in the text, only trajectories for which $T_i\geqslant\tau$ will be counted in the displacements' sample. For a trajectory shorter than τ, the corresponding $\mathbf{D}_i(n)$ is empty and no estimator $\hat{g}(\mathbf{D}_i(n))$ can be computed. The duration of a trajectory T_i is in fact an observation of another random variable whose distribution depends, among other factors, on the dynamics of the corresponding particle. Hence, a particle that is likely to travel across the volume of observation (say its smallest dimension z_{b}; see Fig. 1) over a lag time τ will not be tracked for a sufficient time to perform any computation from its trajectory. The corresponding material in which probes undergo such dynamics will not be detectable by the technique. A proposed quantitative indicator of this effect is *the degree of sampling*, which we define as

$$\theta(n)=\frac{\sum_{i\in I(n)}n_i}{\sum_{i=1}^{N}n_i}.\qquad(5)$$

It is the ratio of the number of positions for which a displacement at lag n has been measured to the total number of observed positions [over which the sum runs in the estimators Eq. (3), where this effect has been discarded by the initial assumptions]. Limiting behaviors of this indicator are reached when all positions are associated with a displacement [$\theta(n)=1$ and the sampling is at its best], and when no sample displacement could be calculated [$\theta(n)=0$ and the material is totally transparent to the technique]. Furthermore, we will show in the following sections that this degree of sampling θ is a good measure to characterize the effect of the volume of observation on the quality of the estimators subsequently derived.

To conclude this section, we notice that this choice of bins $\{V_k\}_{1\leqslant k\leqslant M}$ is not unique. For example, bins of identical shape and size could be chosen to divide V_b independently of the sample $\mathbf{X}$. Their size and number would then need to be adjusted for each lag time to reach the best statistical accuracy. The latter might be challenging to evaluate on the fly. The bins could also be constructed randomly by Voronoi tessellation from a subset of $\mathbf{X}$. The choice made here, relying on the assumption that a particle probes a unique material property along its path, is a more natural procedure in the particle tracking framework (the case where a single, freely diffusing particle encounters liquids of different viscosities along its trajectory has been recently discussed [36]).

In the next two sections, we investigate the second level of statistics involved in the evaluation of $\hat{g}(\mathbf{D}_i(n))$.

B. Characterization of the sample of displacements

For simplicity, we will consider only one-dimensional random walks in the x direction. The output of a multiple particle tracking experiment is a list of one-dimensional overlapping displacements as defined earlier, $D(n) = \{\{d_{i,j}(n) = x_{i,j+n-1} - x_{i,j-1}\}_{1\leqslant j\leqslant q_i(n)}\}_{i\in I(n)}$. Here we look at the characteristics of this sample. If all processes $x_{i,j}$ are assumed stationary with respect to the time j, as well as *independent* of one another (see discussion in the previous section), then we can immediately write the following second-order characterization:

$$\mathbb{E}[d_{i,j}(n)] = 0,$$

$$\mathbb{E}[d_{i,j}^2(n)] = m_i(n),$$

$$\mathbb{E}[d_{i,j}(n)d_{i',j'}(n)]/\mathbb{E}[d_{i,j}^2(n)] = \delta_{ii'}\rho_{n,i}^{(1)}(j-j'),$$

where $\delta_{ii'}$ designates the Kronecker delta and where the correlation coefficient $\rho_{n,i}^{(1)}(h)$ can be expressed in terms of the mean-squared displacement $m_i(n)$ by

$$\rho_{n,i}^{(1)}(h) = \frac{[m_i(h+n) - m_i(h)] + [m_i(h-n) - m_i(h)]}{2m_i(n)}.$$

Under the assumption that all displacements are Gaussian distributed, this second-order characterization is sufficient to know all other moments of the displacement samples. For example, an interesting characteristic when calculating the mean-squared displacement to some power is the correlation coefficient of the squared displacements,

$$\frac{\mathbb{E}[d_{i,j}^2(n)d_{i',j'}^2(n)] - \mathbb{E}[d_{i,j}^2(n)]\mathbb{E}[d_{i',j'}^2(n)]}{\mathbb{E}[d_{i,j}^4(n)] - \mathbb{E}[d_{i,j}^2(n)]^2} = \delta_{ii'}\rho_{n,i}^{(2)}(j-j'),$$

where it can be shown that $\rho_{n,i}^{(2)}(h) = [\rho_{n,i}^{(1)}(h)]^2$. We show typical values of $\rho_n^{(1)}(h)$ in Fig. 2 for various dynamics $m(n)$. We observe that in general the overlapping displacements are correlated up to a nonuniversal lag h. More interestingly, we see on this figure that even if the displacements are not overlapping ($h \geqslant n$), anticorrelations can be observed. In this regard, only the Newtonian dynamics [pure diffusion, $m \propto |n|$ in Fig. 2(a)] exhibit uncorrelated successive displacements. We can conclude then that the observations of the squared displacement will also exhibit correlations in a nonuniversal way.

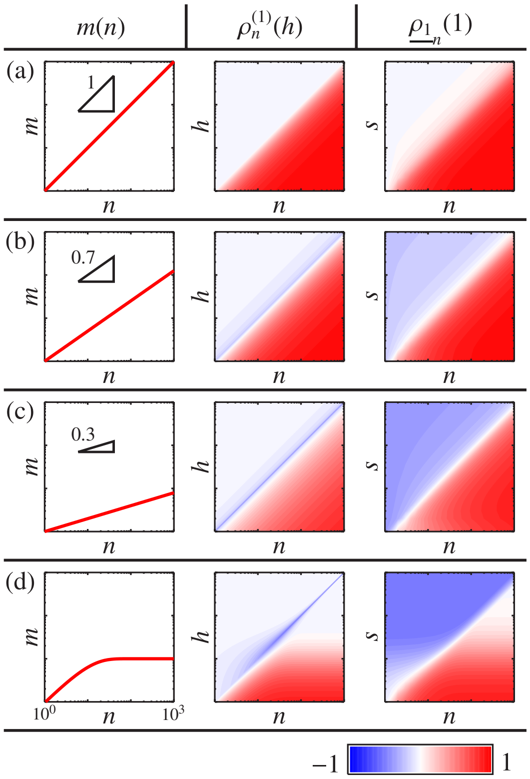

FIG. 2. (Color online) Autocorrelation coefficients of the displacements and the block-averaged displacements. Different dynamics $m(n)$ are investigated: (a) is a purely Newtonian fluid $m(n) \propto |n|$, (b) and (c) are 0.7 and 0.3 power-law dynamics, $m(n) \propto |n|^{0.7}$ and $m(n) \propto |n|^{0.3}$, respectively, and (d) is a Voigt fluid model with relaxation time of 10, $m(n) \propto 1 - e^{-|n|/10}$. The plots on the second column give the displacements' autocorrelation coefficient $\rho_n^{(1)}(h)$ as a function of (n,h) for the corresponding dynamics shown in the first column. The third column of plots shows the autocorrelation coefficient of two successive boxed averaged displacements $\underline{\rho_1}_n(1)$ as a function of (n,s) (see text for notations).

This will present a problem when applying usual estimator formulas involving squared sums of observations. A common way to decorrelate observations is to perform a block-average transformation [37]. We define the s-sized block average of the rth power displacement in the following way:

$$\underline{d_r}_{i,j}(n) = \frac{1}{s}\sum_{l=0}^{s-1} d_{i,sj-l}^r(n).$$

The characteristic of these new observations can also be calculated:

$$\mathbb{E}[\underline{d_r}_{i,j}(n)] = \mathbb{E}[d_{i,j}^r(n)]$$

and

$$\frac{\mathbb{E}[\underline{d}_{r_{i,j}}(n)\underline{d}_{r_{i',j'}}(n)]-\mathbb{E}[\underline{d}_{r_{i,j}}(n)]\mathbb{E}[\underline{d}_{r_{i',j'}}(n)]}{\mathbb{E}[\underline{d}_{r_{i,j}}^{2}(n)]-\mathbb{E}[\underline{d}_{r_{i,j}}(n)]^2}=\delta_{ii'}\underline{\rho}_{r_{n,i}}(j-j'),$$

where we compute the block-averaged transform of the displacement autocorrelation coefficient,

$$\underline{\rho}_{r_{n,i}}(h)=\frac{\displaystyle\sum_{k=-(s-1)}^{s-1}(1-|k|/s)\rho_{n,i}^{(r)}(|h|s+k)}{\displaystyle\sum_{k=-(s-1)}^{s-1}(1-|k|/s)\rho_{n,i}^{(r)}(k)}.$$

We plot in Fig. 2 the correlation $\underline{\rho}_{1_{n,i}}(1)$ of successive block-averaged displacements as a function of s, and we see that the choice $s=n$ decorrelates successive block-averaged displacements. This apparent decorrelation is effectively a smoothing of the raw displacements correlation, that can be observed for higher order correlation coefficient [$\underline{\rho}_{r_n}(h)$ is also almost zero for $r>1$ and for $h\geqslant 1$, even though it is not the case for the corresponding $\rho_n^{(r)}(h)$; data not shown]. A more general definition of the block-averaged rth power displacement is given by

$$\underline{d}_{r_{i,j}}(n)=\frac{1}{s_i(n)}\sum_{l=0}^{s_i(n)-1}d^{r}_{i,s_i(n)j-l},$$

where $s_i(n)=n$ if $q_i(n)\geqslant n$, $s_i(n)=q_i(n)$ otherwise. For each trajectory, we obtain $\underline{q}_i(n)$ block-averaged displacements with $\underline{q}_i(n)$ equal to the biggest integer smaller than $q_i(n)/s_i(n)$. It forms a sample $\underline{D}_r(n)=\{\{\underline{d}_{r_{i,j}}(n)\}_{1\leqslant j\leqslant \underline{q}_i(n)}\}_{i\in I(n)}$ of mutually uncorrelated observations. Note that this choice of $s_i(n)$ does not lead to a significant loss of statistics as compared to calculations made with nonoverlapping displacements. In the latter, approximately n_i/n displacements can be extracted from trajectory i, comparable to $\underline{q}_i(n)$.

C. The estimators

We define the weighted sample mean

$$\overline{d^p}(n)=\sum_{i\in I(n)}\sum_{1\leqslant j\leqslant q_i(n)}w_i(n)d^{p}_{i,j}(n),$$

with $w_i(n)=[n_i/q_i(n)]/\Sigma_{i\in I(n)}n_i$ over the sample $D(n)$. Similarly, we will write

$$\overline{\underline{d}_r^{\,p}}(n)=\sum_{i\in I(n)}\sum_{1\leqslant j\leqslant \underline{q}_i(n)}\underline{w}_i(n)\underline{d}_{r_{i,j}}^{\,p}(n),$$

with $\underline{w}_i(n)=[n_i/\underline{q}_i(n)]/\Sigma_{i\in I(n)}n_i$ over the sample $\underline{D}_r(n)$. In general, $\overline{\underline{d}_r^{\,p}}(n)\neq\overline{d^{rp}}(n)$ unless $p=1$, in which case the two terms differ only by the number of sample displacements lost when taking the integer part of $q_i(n)/s_i(n)$. However, we have $\mathbb{E}[\overline{\underline{d}_r}(n)]=\mathbb{E}[\overline{d^r}(n)]$.

We define the estimator $\widehat{M}_1(n)$ of $M_1(n)=\mathbb{E}[m(n)]$ by

$$\widehat{M}_1(n)=\overline{d^2}(n)=\sum_{i\in I(n)}w_i(n)\sum_{1\leqslant j\leqslant q_i(n)}d^2_{i,j}(n). \tag{6}$$

With $p_i'=n_i/\Sigma_{i\in I(n)}n_i$, the second-level expectation is

$$\mathbb{E}[\widehat{M}_1(n)|\{V_k\}_{1\leqslant k\leqslant M}]=\left(\sum_{i\in I(n)}n_i\right)^{-1}\sum_{i\in I(n)}n_i m_i(n)$$
$$=\sum_{i\in I(n)}p_i' m_i(n),$$

and is unbiased in the first level for $\theta(n)=1$ [see Eq. (3) with $p_i'=p_i$]. If the system is homogeneous, however, $\widehat{M}_1(n)$ is unbiased for any value of $\theta(n)$, as will be shown in the next section.

To calculate the variance of $\widehat{M}_1(n)$, we note that there are two independent contributions in the uncertainty of the estimator, each contribution coming from the two different levels of sampling mentioned earlier in the text. To see this, let us briefly derive a simplified result. We consider a set of N unbiased estimators $\{\hat{a}_i\}_{1\leqslant i\leqslant N}$ of a corresponding set of values $\{\alpha_i\}_{1\leqslant i\leqslant N}$, the latter forming a sample of independent observations of a random variable α. Similar to the current study, we have here two levels of statistical uncertainty when estimating some moments of α: one level is affecting the accuracy of estimating each α_i with $\hat{a}_i$, and the other is coming from the limited number of observations α_i. In the first level, we have $\mathbb{E}[\hat{a}_i|\alpha_i]=\alpha_i$ and we define the variance of the estimator $\hat{a}_i$ by $\mu_2[\hat{a}_i|\alpha_i]=\mathbb{E}[\hat{a}_i^2|\alpha_i]-\mathbb{E}[\hat{a}_i|\alpha_i]^2=\beta_i/n_i$ where n_i is the size of the sample used to calculate $\hat{a}_i$. It can be shown that $\beta_i=O(n_i^0)$ in most cases [38]. We can calculate the mean and variance of the quantity $\hat{a}=N^{-1}\Sigma_{1\leqslant i\leqslant N}\hat{a}_i$ that is an estimator of $\mathbb{E}[\alpha]$. We use the iterated expectation to write

$$\mathbb{E}[\hat{a}]=\mathbb{E}[\mathbb{E}[\hat{a}|\{\alpha_i\}_{1\leqslant i\leqslant N}]]=\mathbb{E}\left[N^{-1}\sum_{1\leqslant i\leqslant N}\alpha_i\right]=\mathbb{E}[\alpha],$$

which shows that the estimator is unbiased. The same way, we find

$$\mathbb{E}[\mathbb{E}[\hat{a}^2|\{\alpha_i\}_{1\leqslant i\leqslant N}]]=\mathbb{E}\left[N^{-2}\sum_{1\leqslant i\leqslant N}\beta_i/n_i+N^{-2}\left(\sum_{1\leqslant i\leqslant N}\alpha_i\right)^2\right]$$
$$=\mathbb{E}[\beta/n]/N+\mu_2[\alpha]/N+\mathbb{E}[\alpha]^2,$$

such that finally the variance of the estimator $\hat{a}$,

$$\mu_2[\hat{a}]=\mu_2[\alpha]/N+\mathbb{E}[\beta/n]/N,$$

is the sum of two terms. The first term comes from the level of sampling of the random variable α with the N observations α_i and is proportional to N^{-1}, and the second term includes the uncertainties from the estimation of each α_i by $\hat{a}_i$ and is of order $(Nn)^{-1}$, where Nn is the total number of initial observations. In the current study, the first term corresponds to the expression given by Eq. (4) for the first level of spatial sampling. The second term can be calculated by assuming the system homogeneous (that is, taking $\mu_2[\alpha]=0$ in the demonstration presented above), which means that all initial observations are taken from the same distribution. Note also that from intermediate calculations in the above demonstration, we get

$$\begin{aligned}\mu_2[\hat{a}|\{\alpha_i\}_{1\leq i\leq N}] &= \mathbb{E}[\hat{a}^2|\{\alpha_i\}_{1\leq i\leq N}] - \mathbb{E}[\hat{a}|\{\alpha_i\}_{1\leq i\leq N}]^2\\ &= N^{-2}\sum_{1\leq i\leq N}\beta_i/n_i \end{aligned} \tag{7}$$

of order $(Nn)^{-1}$. This result will be useful in the following derivations.

We follow this idea to calculate the variance of $\widehat{M}_1(n)$. We use the approximation $\overline{d^2}(n)\approx\overline{\underline{d}_2}(n)$, the mean of the sample $\underline{D}_2(n)$ of uncorrelated observations. In that case, it is possible to show that the variance $\mu_2[\widehat{M}_1(n)]_{\mathrm{h}}$ obtained when all observations in $\underline{D}_2(n)$ are identically distributed (assumption of homogeneity) is equal to $\mu_2[\underline{d}_{2_{i,j}}]\Sigma_{i\in I(n)}\underline{q}_i(n)\underline{w}_i(n)^2$, which is estimated by

$$\hat{\mu}_2[\widehat{M}_1(n)]_{\mathrm{h}} = \frac{[\overline{\underline{d}_2{}^2}(n) - \overline{\underline{d}_2}(n)^2]\sum_{i\in I(n)}\underline{q}_i(n)\underline{w}_i(n)^2}{\sum_{i\in I(n)}\underline{q}_i(n)\underline{w}_i(n)[1-\underline{w}_i(n)]},$$

so that the total expression is [see Eq. (4)]

$$\hat{\mu}_2[\widehat{M}_1(n)] = \frac{\widehat{M}_2(n)}{N_{\mathrm{b}}} + \hat{\mu}_2[\widehat{M}_1(n)]_{\mathrm{h}}, \tag{8}$$

where we have used Eq. (4) with $\widehat{M}_2(n)$ an estimator of $M_2(n)=\mu_2[m(n)]$.

To calculate $\widehat{M}_2(n)$, we assume that all displacements are Gaussian distributed. In that case, we find that

$$\widehat{M}_2(n) = \overline{d^4}(n)/3 - \widehat{M}_1(n)^2 \tag{9}$$

is almost unbiased. Indeed, for the first term in $\widehat{M}_2(n)$, we have

$$\mathbb{E}[\overline{d^4}(n)|\{V_k\}_{1\leq k\leq M}] = 3\frac{\sum_{i\in I(n)} n_i m_i(n)^2}{\sum_{i\in I(n)} n_i}$$

since $\mathbb{E}[d^4]=3\mathbb{E}[d^2]^2$ for a zero-mean Gaussian random variable d. The expectation of the second term can be written

$$\begin{aligned}\mathbb{E}[\widehat{M}_1(n)^2|\{V_k\}_{1\leq k\leq M}] &= \mathbb{E}[\widehat{M}_1(n)|\{V_k\}_{1\leq k\leq M}]^2\\ &\quad + \mu_2[\widehat{M}_1(n)|\{V_k\}_{1\leq k\leq M}],\end{aligned}$$

where the second term is of order $\Sigma_{i\in I(n)}\underline{q}_i(n)\underline{w}_i(n)^2$ from Eq. (7), that is, of the order of the inverse total number of displacements $\Sigma_{i\in I(n)}n_i$ in $D(n)$. This second term can thus be neglected, and we finally get

$$\begin{aligned}\mathbb{E}[\widehat{M}_2(n)|\{V_k\}_{1\leq k\leq M}] &= \sum_{i\in I(n)} p_i'\left[m_i(n) - \sum_{i\in I(n)} p_i' m_i(n)\right]^2\\ &\quad + O\left(\left(\sum_{i\in I(n)} n_i\right)^{-1}\right),\end{aligned}$$

which is the estimate given in Eq. (3) for the first level of uncertainty when $\theta(n)=1$. To estimate $\mu_2[\widehat{M}_2(n)]$ we follow the same line of reasoning as for the variance of $\widehat{M}_1(n)$. We used the software SYMSS [39], relying on the computer algebra package MATHEMATICA (Wolfram Research), to calculate the variance $\mu_2[\widehat{M}_2(n)]_{\mathrm{h}}$ under the homogeneity assumption, and found

$$\begin{aligned}\hat{\mu}_2[\widehat{M}_2]_{\mathrm{h}} = {}&\left(\frac{\overline{\underline{d}_4{}^2} - \overline{\underline{d}_4}^2}{9} + 4\overline{\underline{d}_2}^2(\overline{\underline{d}_2{}^2} - \overline{\underline{d}_2}^2) + \frac{4\overline{\underline{d}_2}}{3}(\overline{\underline{d}_2}\,\overline{\underline{d}_4} - \overline{\underline{d}_2\,\underline{d}_4})\right)\\ &\times\left(\sum_{i\in I(n)} n_i\right)^{-1} + O\left(\left(\sum_{i\in I(n)} n_i\right)^{-2}\right),\end{aligned}$$

where we have dropped the dependency in n for conciseness in the notation (also, we used $\overline{\underline{d}_2\,\underline{d}_4} = \Sigma_{i\in I(n)}\Sigma_{1\leq j\leq \underline{q}_i(n)}\underline{w}_i\underline{d}_{2_{i,j}}\underline{d}_{4_{i,j}}$). The first-level term given by Eq. (4) requires the estimation of $\mu_4[m(n)]$ {the other term $\mu_2[m(n)]$ is estimated by $\widehat{M}_2(n)$}, which is obtained under the Gaussian assumption

$$\hat{\mu}_4[m] = \overline{d^8}/105 - 4\overline{d^2}\,\overline{d^6}/15 + 2\overline{d^2}^2\,\overline{d^4} - 3\overline{d^2}^4,$$

so that finally

$$\hat{\mu}_2[\widehat{M}_2] = (\hat{\mu}_4[m] - \widehat{M}_2^2)N_{\mathrm{b}}^{-1} + \hat{\mu}_2[\widehat{M}_2]_{\mathrm{h}}. \tag{10}$$

II. METHODS

A. Simulations

We used Brownian dynamics simulations to test the validity of the estimator. Simulations are convenient as they provide both freedom of design and a well-defined system. The input parameters are easily changed and well controlled in a wide range of values. However, we must first ensure the validity of this range as compared to real experimental designs.

1. Scaling and range of parameters

The smallest dimension of the volume of observation given in the z direction is called z_{b} (see Fig. 1). Its value depends on the depth of field of the multiple particle tracking technique as well as the tracking parameters. But typical values range from 1 to 10 μm (see Sec. II B). The concentration of probe particles is chosen such that minimal interaction between particles is expected. Given the magnification, between 10 and 100 particles can be tracked simultaneously ($10<N_{\mathrm{b}}<100$). The video rate is usually not greater than 100 Hz; thus the time interval between consecutive frames is $\Delta t>0.01$s. The duration of the movie is limited by the number of frames storable in memory, but typically $T_{\mathrm{b}}=1000\Delta t$. The smallest viscosity encountered in typical applications is that of water $\eta=10^{-3}$ Pa s, and at $T=25$ °C with smallest trackable particle radius $a=0.05$ μm, we get that $\xi=6\pi a\eta>1$ cP μm. Throughout the following sections, we will use quantities made dimensionless with the distance z_{b} and the time Δt. Hence, in the following we will designate the dimensionless quantities using a tilde, such that, for example, $\widetilde{m}=m/z_{\mathrm{b}}^2$ designates the dimensionless mean-squared displacement. However, to avoid redundancy, the dimensionless lag time and acquisition duration are written $n=\tilde{\tau}=\tau/\Delta t$ and $n_{\mathrm{b}}=\tilde{T}_{\mathrm{b}}=T_{\mathrm{b}}/\Delta t$, respectively, as already introduced earlier.

2. Brownian dynamics simulations

A Brownian dynamics simulation was employed to create particle trajectories [40]. An explicit first-order time-stepping algorithm was used to advance the position $\mathbf{x}_j(t)$ of a particle j at time t,

$$\mathbf{x}_j(t+\delta t)=\mathbf{x}_j(t)+\dot{\mathbf{x}}_j(t)\delta t,$$

where δt is the time step and $\dot{\mathbf{x}}_j(t)$ satisfies the following stochastic differential equation:

$$\dot{\mathbf{x}}_j(t)\simeq\frac{1}{\xi_j}\mathbf{F}_j(\mathbf{x}_j(t))+\sqrt{\frac{2k_{\mathrm{B}}T}{\xi_j\delta t}}d\mathbf{W}_j,$$

obtained by assuming the drag on the particle to be Stokesian and by neglecting any other hydrodynamic interactions. Also, $\mathbf{F}_j(\mathbf{x})=-k_j(\mathbf{x}-\mathbf{c}_j)$ is the Hookean linear force law applied to the particle by the medium from the fixed center position $\mathbf{c}_j$ [$\mathbf{F}_j(\mathbf{x})=\mathbf{0}$ when simulating a Newtonian fluid] and $\mathbf{W}_j$ is a Wiener process that satisfies $\langle d\mathbf{W}_j\rangle=\mathbf{0}$ and $\langle d\mathbf{W}_j d\mathbf{W}_j\rangle=\boldsymbol{\delta}$ where $\boldsymbol{\delta}$ is the unit second-order tensor [40]. The model fluid is then characterized by the properties $\nu_j=(\xi_j,k_j)$, and dynamics by $m(\tau)=2k_{\mathrm{B}}T(1-e^{-k_j|\tau|/\xi_j})/k_j$ in each direction. N_{b} trajectories of duration T_{b} were simulated. The effect of the finiteness of the imaging volume is taken into account only in the z direction of the motion $\mathbf{x}(t)=(x(t),y(t),z(t))$, where only positions verifying $0\leqslant z(t)<z_{\mathrm{b}}$ can be observed. In practice, the N_{b} force centers $\{c_j\}_{1\leqslant j\leqslant N_{\mathrm{b}}}$ are uniformly distributed in an interval $[0,z_{\mathrm{b}}]$ in the z direction. About these centers, N_{b} initial positions $\{z_j(0)\}_{1\leqslant j\leqslant N_{\mathrm{b}}}$ are randomly chosen from the equilibrium distribution $P_{z_j(0)}(z)\propto e^{-k_j(z-c_j)^2/(2k_{\mathrm{B}}T)}$. This ensures that the system is at thermal equilibrium at $t=0$. The trajectories are then simulated starting from these positions. For each trajectory $\mathbf{x}_j(t)$, with $1\leqslant j\leqslant N_{\mathrm{b}}$, the first z position that lies outside the box interval $[0,z_{\mathrm{b}}]$ is translated by a length z_{b} to fall back in the observable interval. Accompanying this translation, an index of trajectory is incremented and assigned to the fragment of trajectory starting from this translated point. The process is repeated over time to obtain fragments of the original $\mathbf{x}_j(t)$ as divided by these periodic boundary conditions in the z direction. After performing this transformation to the N_{b} initially simulated trajectories, all the fragments are reindexed to obtain the sample $\{\mathbf{x}_i(t)\}_{1\leqslant i\leqslant N}$ of N tracks. By always keeping all successive positions in the volume of observation, the condition of constant particle density, $\Sigma_{i=1}^{N}T_i=N_{\mathrm{b}}T_{\mathrm{b}}$, is satisfied for all time. For all sets of simulation, $\delta t=10^{-1}\Delta t$. We verified that our results did not appreciably change for smaller values of δt. Allowing the density $N_{\mathrm{b}}(t)$ to fluctuate by observing only a subvolume of height z_{b} in an initial box of height larger than z_{b} is a more detailed model of real multiple particle particle tracking experiments. But again, by doing so, we could not observe significant change in the results, whereas the computation time is increased.

In the following, the friction coefficient and spring constant are made dimensionless by using $\tilde{\xi}=\xi/(k_{\mathrm{B}}T\Delta t/z_{\mathrm{b}}^2)$ and $\tilde{k}=k/(k_{\mathrm{B}}T/z_{\mathrm{b}}^2)$, respectively. From the previous discussion about the range of parameters met in experiments, we conclude that typically $\tilde{\xi}>10$.

B. Experiments

Simple bimodal heterogeneous systems were made by creating gel features in the field of view of the multiple particle tracking setup. We used microscope projection photolithography [41] to create well-defined regions of gel with embedded beads, within a region of purely viscous, unpolymerized material also populated with the probe particles.

We used a solution of 10% (v/v) poly(ethylene glycol)(700) diacrylate (PEG-DA, Sigma-Aldrich), 0.5% (v/v) solutions of Darocur 1173 (Sigma Aldrich) initiator, 20% (v/v) ethanol (95% grade, Pharmco), and 20% (v/v) 5 ×TBE buffer, in which $2a=0.518$ μm diameter carboxylate-modified yellow-green particles (Polysciences) at a volume fraction $\phi=2.48\times10^{-3}\%$ were thoroughly dispersed by 20 min sonication. The sample was injected in a 150-μm-high, custom built chamber of observation sealed with vacuum grease, and mounted on an inverted microscope (Zeiss). Four photomasks with unique pinholes of diameter 470, 700, 800, and 900 μm were designed in AUTOCAD 2005 and printed using a high-resolution printer at CAD Art Services (Poway, CA). The masks were then inserted into the field-stop of the microscope. A 100 W HBO mercury lamp served as the source of uv light. A filter set providing wide uv excitation (11000v2, uv, Chroma) was used to select light of the desired wavelength and a VS25 shutter system (Uniblitz) driven by a computer-controlled VMM-D1 shutter driver provided specified pulses of uv light. The oligomer solutions mixed with probed particles were exposed for a time of 1.5 s to photopolymerize poles in the chamber by using the 10× objective [numerical aperture (NA)=0.25]. It has been shown that the poles are not cylinders of uniform radius because of the shape of the light beam [42]. However, they can be considered as straight cylinders over a length scale of 60 μm around the focal plane of the beam. At this altitude in the chamber, their diameters are respectively $2R_{\mathrm{gel}}=110\pm4$, 170 ± 2, 200 ± 2, and 230 ± 3 μm (this leads to a magnification of approximately 1/4 from the field-stop plane to the objective focal plane). With a 20× objective (NA=0.5), we recorded the motion of the particles in a volume of observation placed such that, within this imaging volume, the poles are straight cylinders at all altitudes $z\in V_{\mathrm{b}}$. The movies were acquired at a rate of ten frames per second (i.e., $\Delta t=0.1$ s) and for a duration of 2000 frames. We verified that the tracking dynamic errors caused by the video interlacing do not affect the validity of the results presented in this study [43]. We also verified that such an exposure time of the solution using the fluorescein-matching fluorescent filter does not induce any photopolymerization. The movies were analyzed offline using the IDL language (Research Systems) tracking package [16]. We find that we track $\langle N_{\mathrm{b}}\rangle\approx250$ particles in a field of view of dimensions 300

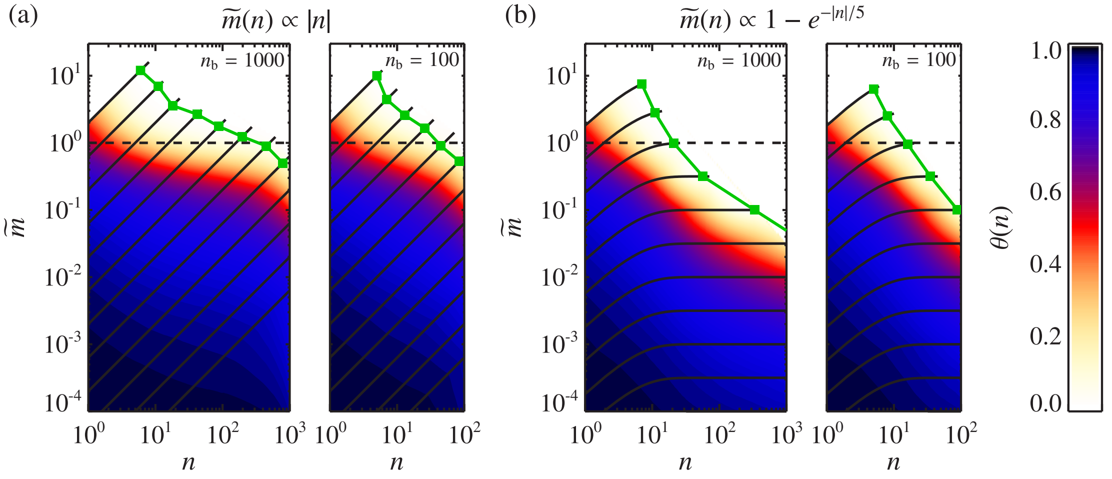

FIG. 3. (Color online) Degree of sampling $\theta(n)$ in the parameter space $(n,\tilde{m})$ scanned by two different kinds of dynamics $\tilde{m}(n)$: (a) is a purely Newtonian fluid, for which $\tilde{m}(n)\propto|n|$, and (b) is a Voigt fluid with relaxation time 5, that is, $\tilde{m}(n)\propto 1-e^{-|n|/5}$. For each fluid type, two acquisition times were simulated, $n_b=1000$ on the left and $n_b=100$ on the right. The dashed line represents the observation limit $\tilde{m}=1$ due to the volume of observation. The connected squares represent the limit above which the relative bias of $\widehat{M}_1$, defined by Eq. (11), is greater than 5%.

$\times 300\ \mu\mathrm{m}^2$, with a standard deviation of less than 5% of this mean $\langle N_b\rangle$. Using $\langle N_b\rangle=C_b x_b y_b z_b$ with $C_b=\phi/[\pi(2a)^3/6]$ and $x_b=y_b=300\ \mu\mathrm{m}$, we can conclude that, for these experiments, using the 20× objective, we have $z_b=8.2\pm0.4\ \mu\mathrm{m}$. Note that this length scale is smaller than the length scale of curvature of the poles' profile in the z direction, ensuring that the polymerized structures are seen as straight cylinders in the experiments.

III. RESULTS AND DISCUSSION

We investigated the quality of the estimator for two different dynamics. The simple diffusive dynamics in Newtonian liquids allow us to scan the parameter space $(n,\tilde{m})$ using the relation $\tilde{m}(n)=2|n|/\tilde{\xi}$ for varying $\tilde{\xi}$. In the single-relaxation-time Voigt fluid, the space $(n,\tilde{m})$ is mapped by changing $\tilde{\xi}$ and $\tilde{k}$ using the following dynamical relation: $\tilde{m}(n)=2(1-e^{-|n|\tilde{k}/\tilde{\xi}})/\tilde{k}$. Admittedly, these two kinds of dynamics do not cover all possible multiple-relaxation-time viscoelastic dynamics often encountered in microrheometry measurements on complex systems. However, they are simple models that are easily implemented with Brownian dynamics simulations, and they exhibit sufficiently different dynamical characteristics to capture the effect of probe dynamics on the quality of the estimators, and more generally on the statistics of the obtained sample.

Before analyzing heterogeneous fluids having these two dynamics, it is instructive to evaluate and characterize the formula in homogeneous fluids.

A. Homogeneous fluids

We performed simulations of homogeneous fluids using $\{\nu_r^{\mathrm{N}}=(\tilde{\xi}_r=10^{r/2},\tilde{k}=0)\}_{0\leq r\leq 11}$ to scan the parameter space $(n,\tilde{m})$ using Newtonian dynamics $\tilde{m}(n)=2|n|/\tilde{\xi}_r$ with different friction coefficients. Also, we used $\{\nu_r^{\mathrm{V}}=(\tilde{\xi}_r=10^{r/2},\tilde{k}_r=10^{r/2}/5)\}_{0\leq r\leq 11}$ to sample the parameter space using Voigt dynamics with a dimensionless relaxation time at $\tilde{\xi}_r/\tilde{k}_r=5$: $\tilde{m}(n)=2(1-e^{-|n|/5})/\tilde{k}_r$. These parameters allow us to investigate $(n,\tilde{m})$ around $\tilde{m}=1$ where the main effects of the finite volume of observation are expected to occur. But their range also report mean-squared displacements sufficiently low, $\tilde{m}\ll 1$, so that the limit in which the volume of observation is infinite is approached. In the simulation method, the latter limit has been separately simulated by discarding the last step consisting of the trajectories subdivision.

For each of the 24 types of fluid (12 Newtonian and 12 Voigt), simulations were repeated 100 times to obtain 100 observations of the various random parameters of interest. These include the largest lag time $n_{\max}$ for which it is possible to calculate the estimators [chosen such that there remains at least two indices in the set $I(n_{\max})$], the degree of sampling $\theta(n)$, and the estimators $\widehat{M}_1(n)$ and $\widehat{M}_2(n)$. From the 100 simulations performed under identical conditions, these observations are calculated at common values of lag time from one simulation to another, so that statistics (mean and standard deviation) for each measure are calculated for a given n.

Figure 3 gives an overview of the results obtained for homogeneous fluids with $N_b=100$ and for two acquisition times $n_b=1000$ and 100. In particular, it shows the mapping of the degree of sampling in the parameter space $(n,\tilde{m})$ for the two kinds of dynamics. In this figure, each solid black line represents the relation $\tilde{m}(n)$ used in the simulations to map the space, $\tilde{m}(n)\propto|n|$ for (a) and $\tilde{m}(n)\propto 1-e^{-|n|/5}$ for (b), and their end points (the maximum n at which they are drawn) is at $\mathbb{E}[n_{\max}]$.

First, we see that for mean-squared displacements above the observation limit $\tilde{m}=1$, the degree of sampling vanishes for both kinds of dynamics. This result is not surprising, as

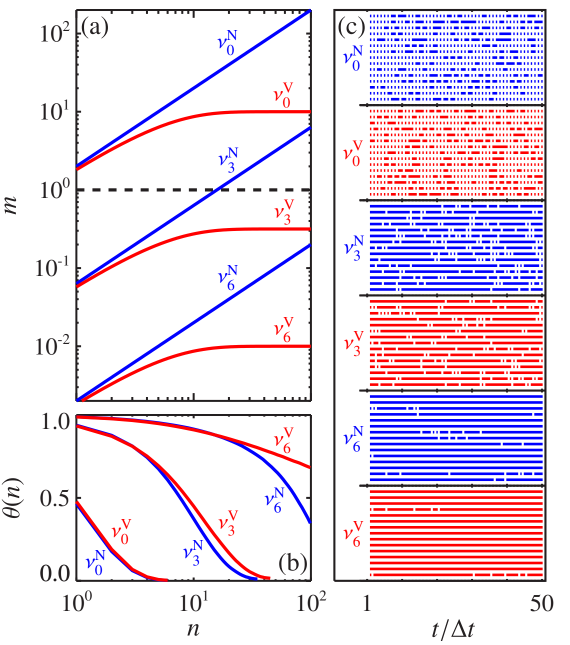

FIG. 4. (Color online) Trajectory statistics. As shown in (a), the parameter space $(n,\widetilde{m})$ is sampled using purely viscous dynamics with material properties $\{\nu_r^{\mathrm{N}}\}_{r\in\{0,3,6\}}$ and Voigt dynamics with relaxation time 5, $\{\nu_r^{\mathrm{V}}\}_{r\in\{0,3,6\}}$ (see the labels on the figure). In (a), the dashed line represents the observation limit $\widetilde{m}=1$ due to the volume of observation. (b) shows the corresponding variations of the degree of sampling $\theta(n)$ as a function of n for each fluid. (c) represents typical trajectory durations: a single dot means that the particle was observable for only one frame, and lines indicate trajectories of at least Δt long. Each line in these plots refers to the original simulated trajectory that has been fragmented to take limited observation volume into account (see Sec. II A 2), and we present results for the two kinds of fluid from top to bottom with increasing values of the index r.

for such values of mean-squared displacement, the probes are more likely to cross the entire volume of observation over a time less than the lag time. Hence a particle in the box at a given time t is likely to be outside the volume of observation at a time $t+\tau$, and thus its observed trajectory cannot be used to extract a displacement at lag time τ.

More strikingly, we see that the degree of sampling in a material where probes have a mean-squared displacement $\widetilde{m}$ at a lag time n depends on the entire dynamics relation $\widetilde{m}(n)$ and not only on the position $(n,\widetilde{m})$ in the parameter space [compare the different mappings of Figs. 3(a) and 3(b)]. This dependency may seem surprising, in particular for the Voigt fluid where some values of $(n,\widetilde{m})$ are undetectable $[\theta(n)\approx 0]$ even though $\widetilde{m}\ll 1$. To provide some insights into this effect, we show in Fig. 4 typical trajectory durations n_i in a selection $\{\nu_r^{\mathrm{N}}\}_{r\in\{0,3,6\}}$ of Newtonian dynamics and $\{\nu_r^{\mathrm{V}}\}_{r\in\{0,3,6\}}$ of Voigt dynamics, as well as the resulting variation $\theta(n)$ of the degree of sampling with the lag time n, for $N_{\mathrm{b}}=100$ and $n_{\mathrm{b}}=100$. Figure 4(c) was obtained by gathering together on the same line the trajectories coming from the same initial simulated trajectory, subsequently chopped when taking the effect of a finite volume of observation into account. Thus, in these plots, a line corresponds to one of the N_{b} simulated particles, and the chopping of this line occurs at the successive absolute times when the corresponding particle crosses one of the observation volume's z boundaries. From $r=0$ to 6, we observe that trajectories are becoming longer, or, equivalently, that the particles are leaving the volume of observation less frequently: from a given position in the volume of observation, slower particles (lower $\widetilde{m}$ at constant n) will not be as likely to reach a given boundary than faster particles (higher value of $\widetilde{m}$ for the same n). Consequently, the degree of sampling at a given lag time n will increase from faster (higher $\widetilde{m}$) to slower (lower $\widetilde{m}$) dynamics, as seen in Fig. 4(b). Also, for each value of r, since the Voigt dynamics are "slower" than the corresponding Newtonian dynamics, we also verify in Fig. 4(b) that the curve for the degree of sampling in Newtonian fluids falls below the corresponding curve for Voigt fluids with same value of r. The peculiarity of the detectability is, however, visible by comparing the Newtonian dynamics ν_6^{N}, $\widetilde{m}(n)=2|n|/10^3$, and the Voigt dynamics ν_3^{V}, $\widetilde{m}(n)=(1-e^{-|n|/5})/10^{1/2}$. At a lag time $n=100$, both exhibit similar values of $\widetilde{m}$ [see Fig. 4(a)] whereas the corresponding degrees of sampling are remarkably different, as seen in Fig. 4(b). Thus the degree of sampling, and hence the detectability, does not depend only on the particular value of $\widetilde{m}$, but rather on the function $\widetilde{m}(n)$ that describes the dynamics of the probes in the entire range of lag times n. The undetectability of certain fluids with multiple particle tracking is an important limitation of the technique. But the dynamic dependency of this detectability is a particularly strong weakness that prevents some universality in judging *a priori* the feasibility of an experiment.

We also report in Fig. 3 the relative bias of the first estimator $\widehat{M}_1(n)$, defined as follows:

$$b[\widehat{M}_1(n)]=\mathbb{E}[\widehat{M}_1(n)]/M_1(n)-1, \tag{11}$$

where the above expected value is calculated from the 100 experiments repeated for each kind of fluid. For these homogeneous fluids, a bias of less than 5% is measured for almost the entire observed parameter space. In particular, it is not affected by the drop in the degree of sampling of the material. In a wide part where the fluid is almost totally undetectable ($\theta\ll 1$), but where the mean-squared displacement can be reported, the bias is negligible. This is not surprising for homogeneous fluids, since any observed displacement will report a valid measurement of the entire fluid. However, we will show in the next part how the bias is greatly affected by the nonuniform detectability of heterogeneous fluids. We also observed that the estimator $\widehat{M}_2(n)$ is unbiased for this kind of fluid. We defined, for this section only, the bias of $\widehat{M}_2(n)$ relative to $M_1^2(n)$ by

$$b'[\widehat{M}_2(n)]=\mathbb{E}[\widehat{M}_2(n)]/M_1^2(n),$$

and we saw that the trends followed by this bias (not reported here) are very similar to the one followed by $b[\widehat{M}_1(n)]$. That is, $\widehat{M}_2(n)$ is unbiased for almost all the observable parameter space [the ensemble of points $(n,\widetilde{m})$ for which $\theta>0$]. Finally, we observe that these qualitative behaviors are not significantly changed when decreasing n_{b} from 1000 to 100 (see Fig. 3) or when decreasing N_{b} from 100 to 10 (not shown).

B. Heterogeneous fluids

We use now the two model fluids, Newtonian and Voigt, mentioned in the previous part to build heterogeneous fluids. Rather than trying to cover a wide variety of heterogeneous fluids, we will use a canonical model of a heterogeneous fluid to point out the influence of a finite volume of observation on measurements. The study of these simple systems, performed using both simulations and experiments, will be followed by a model fluid with a more complex heterogeneous nature, which will illustrate the power of the formula.

1. Bimodal fluids

A canonical model for a heterogeneous fluid is given by a balanced bimodal system, where the fluid is composed of half of one kind and half of another kind. More precisely, we define a set of balanced bimodal Newtonian fluids where half of the volume of observation is occupied with a liquid of friction $\tilde{\xi}_r=10^{r/2}$, and the other half exhibits a friction $\tilde{\xi}_{r+1}=10^{(r+1)/2}$, where $0\leqslant r\leqslant 10$. The resulting equally likely probe dynamics are written $\tilde{m}^{(1)}(n)=2|n|/\tilde{\xi}_r$ and $\tilde{m}^{(2)}(n)=2|n|/\tilde{\xi}_{r+1}$, and the heterogeneous fluid will be denominated $\nu_r^{\mathrm{N}}+\nu_{r+1}^{\mathrm{N}}$. Similarly, a set of bimodal Voigt fluids is built from a balanced mixture of $(\tilde{\xi}_r=10^{r/2},\tilde{k}_r=10^{r/2}/5)$ on one side and $(\tilde{\xi}_{r+1}=10^{(r+1)/2},\tilde{k}_{r+1}=10^{(r+1)/2}/5)$ on the other side with $0\leqslant r\leqslant 10$, and will lead to the two equally likely dynamics $\tilde{m}^{(1)}(n)=2(1-e^{-|n|/5})/\tilde{k}_r$ and $\tilde{m}^{(2)}(n)=2(1-e^{-|n|/5})/\tilde{k}_{r+1}$. The latter fluid will be referred to as $\nu_r^{\mathrm{V}}+\nu_{r+1}^{\mathrm{V}}$. Looking at Fig. 3, we see that the described bimodal fluids are made of a balanced composite of two successive dynamics represented by the black solid lines. The estimators $\widehat{M}_1(n)$ and $\widehat{M}_2(n)$ are built to evaluate

$$\widetilde{M}_1(n)=\frac{\tilde{m}^{(1)}(n)+\tilde{m}^{(2)}(n)}{2},$$

$$\widetilde{M}_2(n)=\frac{[\tilde{m}^{(1)}(n)-\tilde{m}^{(2)}(n)]^2}{4}$$

in these models.

In the simulation method, these fluids are obtained by simulating 50 initial trajectories in one homogenous component of the fluid, and then 50 trajectories in the other component. The effect of the limited volume of observation is taken into account in the same way as described in Sec. II A 2. In practice, an experiment in such a hypothetical fluid should be simulated by assigning random initial positions for each trajectory, uniformly distributed through the heterogeneous fluid. Hence, by exactly splitting the trajectory set in half, we discard in this part the random spatial sampling. It is aimed at isolating a specifically strong limitation of the method: the effect of detectability on the bias of the estimators. In the experiments described in the next section, the spatial sampling is naturally performed.

Referring again to Fig. 3, we observe that, in general, along the lines representing the two dynamics involved in the bimodal fluid, the drop in the degree of sampling is reached at different values of n and $\tilde{m}$. The dynamics exhibiting higher $\tilde{m}$, that is, $\tilde{m}^{(1)}$, will eventually become undetectable at smaller lag time, and the tracking technique will then only probe the remaining observable side of the heterogeneous fluid at larger lag time. Consequently, the estimators of the mean and variance of the probes' dynamics will be biased for these large lag times.

To be more precise, we want to compare the detectability map θ as scanned by dynamics in the fluid of type 1, for which the mean-squared displacement is $\tilde{m}^{(1)}(n)$, with a map of the estimators' bias as scanned by the composite dynamics described by $\widetilde{M}_1(n)$. To perform this comparison quantitatively, we juxtapose in Figs. 5(a) and 5(b) the behavior of the levels of constant value of θ, with levels of constant bias of $\widehat{M}_1(n)$ and $\widehat{M}_2(n)$ in the $(n,\tilde{m})$ space. The bias is defined here for both estimators using Eq. (11),

$$b[\widehat{M}_i(n)]=\mathbb{E}[\widehat{M}_i(n)]/M_i(n)-1 \quad \text{for } i=1,2,$$

and is visible in Figs. 5(a) and 5(b) by comparing the theoretical composite dynamics $\widetilde{M}_1(n)$ (black solid lines in these figures) with the estimator $\widehat{M}_1(n)$ (dash-dotted lines). Note how $\widehat{M}_1(n)$ tends to $\tilde{m}^{(2)}(n)$ (see labeled dashed line) as the dynamics $\tilde{m}^{(1)}(n)$ of fluid 1 becomes less detectable, as explained above.

More specifically, we used the result for the degree of sampling obtained in homogenous fluid of kind 1 to uniquely read the coordinates $(n_\theta,\tilde{m}_\theta)$ on the corresponding curve $\tilde{m}_\theta=\tilde{m}^{(1)}(n_\theta)$ at which detectability reaches a given value θ [the triangles in Figs. 5(a) and 5(b) are at $(n_\theta,\tilde{m}_\theta)$ for $\theta=0.5$]. Then, at the same lag time n_θ, we read the bias of the estimators at the point $(n_\theta,\widetilde{M}_1(n_\theta))$ [the diamonds in Figs. 5(a) and 5(b) are at $(n_\theta,\widetilde{M}_1(n_\theta))$ for $\theta=0.5$]. Next, by varying r, we obtained a curve of constant degree of sampling [the solid lines connecting the triangles in Figs. 5(a) and 5(b) are extracted from the contour plots given in Fig. 3] for the fluid of kind 1, and a corresponding set of bias values on the associated composite dynamics $\widetilde{M}_1(n)$. The mean of this set of bias values was calculated for a given degree of sampling, and is reported in Figs. 5(c) and 5(d) for varying values of θ, the error bars being given by the standard deviation of the same set. If these error bars are small, it means that to a given value of detectability of fluid 1 corresponds a well-defined value of bias in the estimator.

To compare with other methods of calculation of the moments of dynamics, we also reported in Figs. 5(c) and 5(d) calculations of the mean and variance of prior time averaged individual mean-squared displacements extracted from each trajectory [14,31,32]. The latter methods completely disregard eventual differences in trajectory durations (hence an apparent statistical heterogeneity in the accuracy of the individual mean-squared displacement estimations). For these estimates, we repeated the study described in the previous

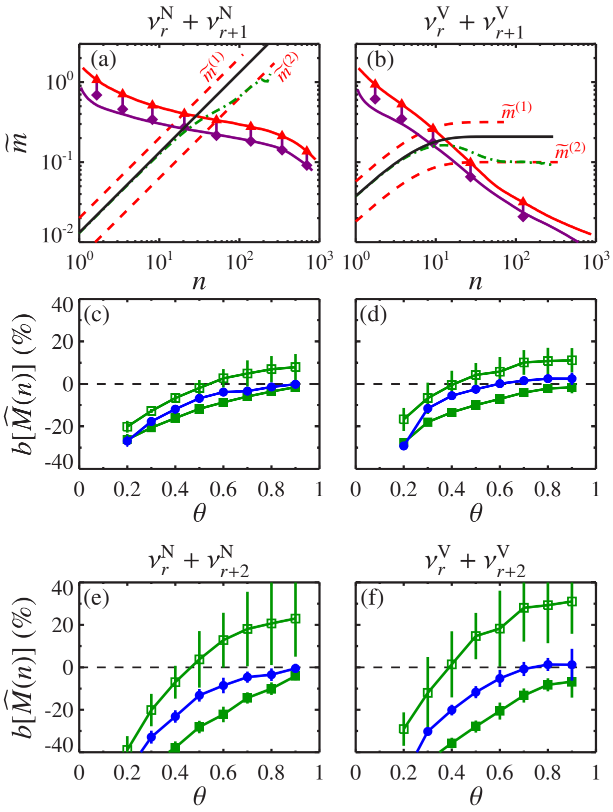

FIG. 5. (Color online) Bias as a function of the degree of sampling θ. The first column of plots (a), (c), and (e) corresponds to a mapping of the parameter space $(n,\widetilde{m})$ using Newtonian dynamics and the second column is for a Voigt fluid. (a) and (b) show the relation between the degree of sampling of the homogeneous fluid 1 (the line connecting the triangles corresponds to a constant $\theta=0.5$) with the bias [the line connecting the diamonds is a constant level of bias for $\widehat{M}_1(n)$] in the bimodal mixtures $\nu_r^N+\nu_{r+1}^N$ (a) and $\nu_r^V+\nu_{r+1}^V$ (b). Refer to the text for further explanations on how these lines are built. The composite fluid [$\widetilde{M}_1(n)$ is given by the black solid line] is made of a balanced mixture of two successive dashed lines, $\widetilde{m}^{(1)}(n)$ and $\widetilde{m}^{(2)}(n)$. The estimator $\widehat{M}_1(n)$ is given by the dash-dotted line. (c) and (d) show the bias in $\widehat{M}_1$ (squares) and $\widehat{M}_2$ (circles) as a function of θ. (e) and (f) show the variation of the bias for a bimodal fluid with greater difference in the dynamics $\nu_r^N+\nu_{r+2}^N$ and $\nu_r^V+\nu_{r+2}^V$, respectively. In (c)–(f), the open symbols are obtained using a prior time averaging for the corresponding estimators (see text). Note that the open circles, corresponding to an estimation of $\widetilde{M}_2$ with prior time averages on individual tracks, lie above 100%, outside the range of bias shown here.

paragraph and the results are given by the open symbols in Figs. 5(c) and 5(d).

In this figure, we see that as θ increases the bias of each estimator derived in this study vanishes. This is not the case for the calculations with prior time averages on individual trajectories as described above. Also, we remark that the error bars on each point are small compared with the ones on the open symbols, indicating that the degree of sampling defined by Eq. (5) in the first section is well correlated with the bias in the estimators. Note finally that the variation of the biases with the degree of sampling is fairly independent of the nature of the dynamics involved, Newtonian or Voigt. The last two plots, Figs. 5(e) and 5(f), show the results corresponding to balanced bimodal fluids with greater differences in the dynamics: $\nu_r^N+\nu_{r+2}^N$ designates a fluid where $\widetilde{\xi}_r=10^{r/2}$ is mixed with $\widetilde{\xi}_{r+2}=10^{r/2+1}$ for the Newtonian dynamics, and $\nu_r^V+\nu_{r+2}^V$ is for a bimodal fluid with $(\widetilde{\xi}_r=10^{r/2},\widetilde{k}_r=10^{r/2}/5)$ and $(\widetilde{\xi}_{r+2}=10^{r/2+1},\widetilde{k}_{r+2}=10^{r/2+1}/5)$ for the Voigt dynamics. We observe that the same conclusions still hold, although the reported biases are significantly higher.

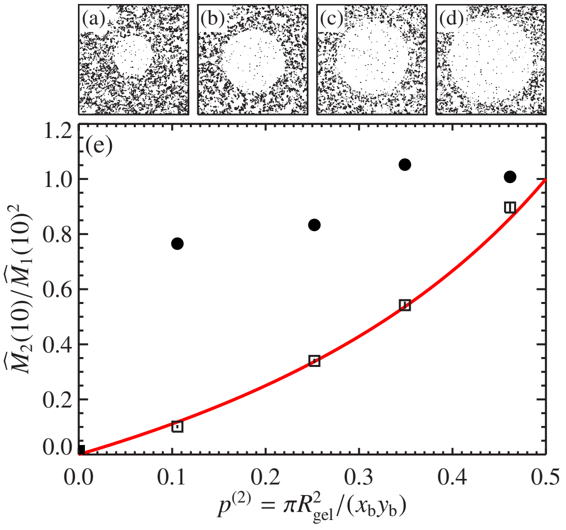

FIG. 6. (Color online) (a)–(d) are the measured trajectories in a heterogeneous unbalanced bimodal model experimental fluid. Each image has dimensions $x_b=y_b=300$ μm. The centered circular gelled region, where the particles are trapped, have radii $R_{\rm gel}=55$, 85, 100, and 115 μm, respectively, from (a) to (d). (e) is the squared coefficient of variation of the probes' dynamics in these fluids. The open squares are estimates of the measure $\mu_2[\widetilde{m}(n)]/\mathbb{E}[\widetilde{m}(n)]^2$ using $\widehat{M}_2(n)/\widehat{M}_1(n)^2$ for the four bimodal fluids created by photopolymerization at $n=10$. The filled square was obtained in the homogeneous system $R_{\rm gel}=0$. The solid line is the theoretical curve, Eq. (12). The circles are the calculations of the squared coefficient of variation using prior time averages on individual tracks (as explained in the previous section about the simulated bimodal fluids; see also Fig. 5).

In the remaining, we will use an experimental unbalanced bimodal system and also simulate a complex and random heterogeneous fluid. To show the strength of the estimators, we will place these studies in conditions where the fluid is almost entirely detectable.

2. Experimental bimodal fluid

As explained in Sec. II, the experimental bimodal fluid is composed of a region of viscous non-cross-linked oligomer solution, and a cylindrical region of known radius where the material is a stiff gel. In Figs. 6(a)–6(d), we show the trajectories extracted from these experiments, where we see that immobile particles are found in the circular region at the center, with varying radius. Around the gelled area, the particles' motion is not constrained. By performing multiple particle tracking on a homogeneous gel system, we observed that the motion of the beads in the gel is below spatial resolution, such that the effective mean-squared displacement is constant and measured at $m(\tau)=5\times10^{-4}$ μm^2 [44]. In the other kind, particles are freely diffusing and we found a diffusion coefficient $D=0.25\pm0.005$ μm^2 s^{-1}. At unit distance $z_b=8.2$ μm and unit time $\Delta t=0.1$ s (see Sec. II), we have an unbalanced bimodal fluid with $\tilde{m}^{(1)}(n)=2|n|/10^{3.44}\gg\tilde{m}^{(2)}(n)=2/10^{5.43}$ at all observed lag times n. Each fluid is observed with respective probabilities $p^{(1)}=1-p^{(2)}$ and $p^{(2)}=\pi R_{\text{gel}}^2/(x_b y_b)$. In that case, we can show that the squared coefficient of variation is given by

$$\frac{\mu_2[m(\tau)]}{\mathbb{E}[m(\tau)]^2}=\frac{M_2(n)}{M_1(n)^2}=\frac{p^{(2)}}{1-p^{(2)}}+O\left(\frac{\tilde{m}^{(2)}}{\tilde{m}^{(1)}}\right). \tag{12}$$

We estimate the above quantity using $\widehat{M}_2(n)/\widehat{M}_1(n)^2$. The lag time n is chosen such that the degree of sampling of fluid 1 is closer to 1. From Fig. 3, we evaluate that θ significantly drops at about $n=100$, in accordance with what we observed in experiments on the homogeneous fluid of kind 1 (data not shown). We evaluated in Fig. 6(e) the ratio $\widehat{M}_2(n)/\widehat{M}_1(n)^2$ at $n=10$ to discard any bias from an eventual undetectability of fluid 1. At this lag time, we found an excellent agreement between the estimator of the squared coefficient of variation and the theoretical value given by Eq. (12) for the whole range of reported $p^{(2)}$. On Fig. 6(e), the error bars on the experimental points (open squares) were calculated using Eqs. (8) and (10), whose validity is demonstrated in the next section. In contrast with the accuracy of the estimators derived in this paper, the evaluation of the squared coefficient of variation, using estimators of $\mu_2[m(\tau)]$ and $\mathbb{E}[m(\tau)]$ calculated with a prior time average on individual trajectory (see description above), reports poor estimates (see the circles in Fig. 6). This illustrates the importance of the characterization and understanding of the sampling design in multiple particle tracking measurements.

3. Random fluid

To conclude the characterization of the estimators, we simulated a random heterogeneous fluid the following way. Each probe undergoes purely Voigt dynamics, $\tilde{m}(n)=2(1-e^{-|n|\tilde{k}/\tilde{\xi}})/\tilde{k}$, where the parameters $\tilde{\xi}$ and $\tilde{k}$ are independently distributed according to the following uniform and Gamma probability density functions: $P_{\tilde{\xi}}(x)=(10^5-10^4)^{-1}$ for $10^4\leqslant x\leqslant10^5$ (0 otherwise), and $P_{\tilde{k}}(x)=4xe^{-2x/10^4}/10^8$ for $0\leqslant x$ (0 otherwise). In particular, random values of $\tilde{k}$ are generated using the expression $\tilde{k}=-\ln(U_1U_2)\times10^4/2$, where $0<U_1,U_2<1$ are random variates drawn from the uniform standard distribution. We simulated 300 initial trajectories in a volume of observation whose z dimension is $3z_b$, but only positions in $[z_b,2z_b]$ were counted to build the trajectory. Hence we let $N_b(t)$ fluctuate in time around a constant value near 100 (see Sec. II). Thus this simulates more realistic experimental measurements. We compare in Fig. 7 the estimators $\widehat{M}_1$ and $\widehat{M}_2$, and the theoretical results for $\tilde{M}_1$ and $\tilde{M}_2$, respectively, whose expressions are given below:

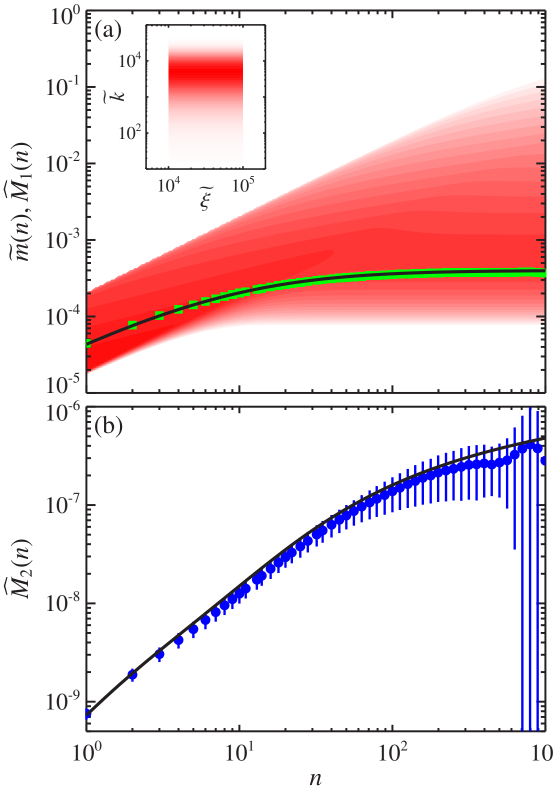

FIG. 7. (Color online) Estimators $\widehat{M}_1$ and $\widehat{M}_2$ calculated for a random fluid. For the random fluid simulated here, the parameter space $(n,\tilde{m})$ is sampled with purely Voigt dynamics for which the drag coefficient $\tilde{\xi}$ is uniformly distributed between 10^4 and 10^5, and the spring constant $\tilde{k}$ is Gamma distributed with mean 10^4 and a shape parameter of 2 ($\tilde{\xi}$ and $\tilde{k}$ are statistically independent). The resulting probability density of $(n,\tilde{m})$ is given (a), where the occurrence is color coded from light to dark for increasing likelihood. The inset of (a) displays the probability density $P_{\tilde{\xi},\tilde{k}}$ following the same color-code convention. In (a), the solid line indicates the mean $\tilde{M}_1$ and the squares report the corresponding estimate $\widehat{M}_1$. (b) compares the results of $\widehat{M}_2$ (circles) obtained by the simulations with the theoretical values $\tilde{M}_2$ (solid line). Error bars for both $\widehat{M}_1$ and $\widehat{M}_2$ were calculated using Eqs. (8) and (10), respectively (see Fig. 8).

$$\tilde{M}_1(n)=\frac{2n}{9\times10^4}\ln\left(\frac{20+n}{2+n}\right),$$

$$\tilde{M}_2(n)=\frac{16n}{9\times10^8}\ln\left(\frac{(1+n)^{n+1}(1+n/20)^{n+20}}{(1+n/2)^{n+2}(1+n/10)^{n+10}}\right)-\tilde{M}_1(n)^2.$$

As seen in Fig. 7, we again find a good agreement between the estimators and their theoretically expected values over the range of lag times n investigated here. Small deviations are visible at high lag times in Fig. 7(b), where eventually undetectability of the faster dynamics in the fluid, for which the mean-squared displacement approaches the volume size limit z_b^2, can alter the bias of the estimators.

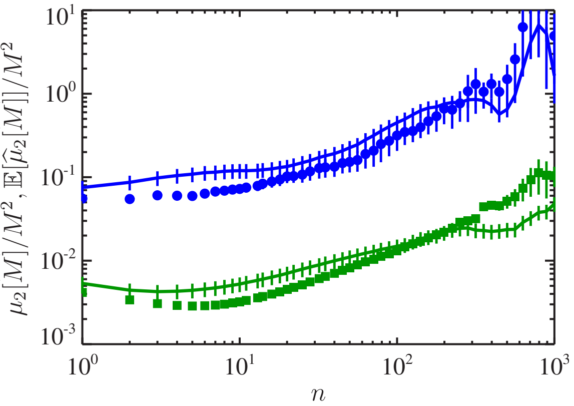

FIG. 8. (Color online) Estimators $\hat{\mu}_2[\widehat{M}_1]$ (squares) and $\hat{\mu}_2[\widehat{M}_2]$ (circles) calculated for the random fluid in Fig. 7 and scaled by the squared mean $M_1^2=\mathbb{E}[m]^2$ and the squared variance $M_2^2=\mu_2[m]^2$, respectively. The associated solid lines are the correspondingly scaled estimates of $\mu_2[\widehat{M}_1]$ and $\mu_2[\widehat{M}_2]$ obtained from repeating the simulation 100 times (the vertical lines are error bars).

For this advanced example, we plot in Fig. 8 the estimators $\hat{\mu}_2[\widehat{M}_1]$ [Eq. (8)] and $\hat{\mu}_2[\widehat{M}_2]$ [Eq. (10)] for the variances of $\widehat{M}_1$ and $\widehat{M}_2$, respectively. In this figure, we also report the corresponding estimates of $\mu_2[\widehat{M}_1]$ and $\mu_2[\widehat{M}_2]$ obtained from the set of 100 simulations performed for the same random fluid (solid lines). We see on this figure a good agreement between the two estimates, ensuring the validity of the expressions of $\hat{\mu}_2[\widehat{M}_1]$ and $\hat{\mu}_2[\widehat{M}_2]$ derived in Sec. I C. Small differences, although almost consistently within the error bars reported in the figure (these error bars were obtained by direct calculations of the sample variance of the sets of observations), could come from residual correlations in the sample between block-averaged displacements (see Fig. 2), but also from statistical uncertainty in estimating $\mu_2[\widehat{M}]$ from the finite-sized set of 100 observations. The accuracy of $\hat{\mu}_2[\widehat{M}]$ is not critical, however, these estimators being used to indicate error bars on $\widehat{M}_1$ and $\widehat{M}_2$ (as performed in Figs. 6 and 7). Similar agreements between $\hat{\mu}_2[\widehat{M}]$ and $\mu_2[\widehat{M}]$ have been observed for all simulation results reported throughout this paper.

IV. CONCLUSIONS

Multiple particle tracking experiments return a list of Brownian probe trajectories. From this output, a sample of displacements is extracted to calculate statistical quantities revealing the properties of the probed material. We outlined here that the sample of displacements presents several peculiarities in a spatially heterogeneous system. If not carefully taken into account, these peculiarities can bias classical estimations of the aforementioned statistical quantities. We presented a description of the sampling design of the multiple particle tracking measurements. This description allowed us to derive the main results of this paper: Eq. (6) estimates the ensemble-averaged mean-squared displacement, a widely used quantity to characterize the spatially averaged mechanical property of the material, and Eq. (8) is used to evaluate the error bars affecting the latter quantity; Eq. (9) gives the ensemble spatial variance of the individual probes' mean-squared displacements, which is a valid and intelligible indicator of the material's heterogeneity, and Eq. (10) can then be used to calculate its error bars. We expect that these formulas will become standard routines to analyze multiple particle tracking data. Moreover, if a material is found to be heterogeneous, we showed an important limitation of the technique coming from undersampling regions in the material where the thermal motion of the embedded probes is allowed to exhibit fluctuations larger than the tracking depth. We called this effect detectability, quantified through the degree of sampling, and showed its influence when attempting to calculate material properties with video microscopy particle tracking. For example, when particles are tracked to assess the micromechanical mapping of live cells, an analysis of individual mean-squared displacements indicates a significant heterogeneity of the cytoplasm [19]. Some probes can reach low-frequency fluctuations of amplitudes close to the depth of tracking of the setup (see results in Ref. [19] obtained with high microscope magnification, leading to small $z_b \sim 1\,\mu$m). Thus in this important application of the video particle tracking technique, special attention should be paid when tentatively applying the estimators derived in this paper.

Overall, this study shows that great care should be allocated to understanding the experimental output of the technique when calculating statistical quantities. Notably, we provided here an initial pathway to further this understanding.

ACKNOWLEDGMENTS

The authors thank P. T. Underhill and K. Titievsky for insightful discussions, and K. M. Schultz for her help with experiments. This material is based upon work supported by the National Science Foundation under Grants No. 0239012 and No. 0304128 (NSF-NIRT).

---

[1] J. Quintanilla, Polym. Eng. Sci. **39**, 559 (1999).
[2] Y. Tseng, K. M. An, and D. Wirtz, J. Biol. Chem. **277**, 18143 (2002).
[3] Y. Tseng and D. Wirtz, Phys. Rev. Lett. **93**, 258104 (2004).
[4] K. Luby-Phelps, P. E. Castle, D. L. Taylor, and F. Lanni, Proc. Natl. Acad. Sci. U.S.A. **84**, 4910 (1987).
[5] K. Luby-Phelps, F. Lanni, and D. L. Taylor, Annu. Rev. Biophys. Biophys. Chem. **17**, 369 (1988).
[6] C. S. Chen, M. Mrksich, S. Huang, G. M. Whitesides, and D. E. Ingber, Science **276**, 1425 (1997).

[7] C.-M. Lo, H.-B. Wang, M. Dembo, and Y.-l. Wang, Biophys. J. **79**, 144 (2000).

[8] S. Gheorghiu and M.-O. Coppens, Proc. Natl. Acad. Sci. U.S.A. **101**, 15852 (2004).

[9] N. D. Gershon, K. R. Porter, and B. L. Trus, Proc. Natl. Acad. Sci. U.S.A. **82**, 5030 (1985).

[10] N. Pernodet, M. Maaloum, and B. Tinland, Electrophoresis **18**, 55 (1997).

[11] W. W. Graessley, *Polymeric Liquids & Networks: Structure and Properties* (Garland Science, New York, 2003).

[12] A. R. Kannurpatti, K. J. Anderson, J. W. Anseth, and C. N. Bowman, J. Polym. Sci., Part B: Polym. Phys. **35**, 2297 (1997).

[13] F. C. MacKintosh and C. F. Schmidt, Curr. Opin. Colloid Interface Sci. **4**, 300 (1999).

[14] J. Apgar, Y. Tseng, E. Fedorov, M. B. Herwig, S. C. Almo, and D. Wirtz, Biophys. J. **79**, 1095 (2000).

[15] M. T. Valentine, P. D. Kaplan, D. Thota, J. C. Crocker, T. Gisler, R. K. Prud'homme, M. Beck, and D. A. Weitz, Phys. Rev. E **64**, 061506 (2001).

[16] J. C. Crocker and D. G. Grier, J. Colloid Interface Sci. **179**, 298 (1996).

[17] I. M. Tolić-Nørrelykke, E.-L. Munteanu, G. Thon, L. Oddershede, and K. Berg-Sørensen, Phys. Rev. Lett. **93**, 078102 (2004).

[18] D. T. Chen, E. R. Weeks, J. C. Crocker, M. F. Islam, R. Verma, J. Gruber, A. J. Levine, T. C. Lubensky, and A. G. Yodh, Phys. Rev. Lett. **90**, 108301 (2003).

[19] Y. Tseng, T. P. Kole, and D. Wirtz, Biophys. J. **83**, 3162 (2002).

[20] A. Goodman, Y. Tseng, and D. Wirtz, J. Mol. Biol. **323**, 199 (2002).

[21] J. H. Shin, M. L. Gardel, L. Mahadevan, P. Matsudaira, and D. A. Weitz, Proc. Natl. Acad. Sci. U.S.A. **101**, 9636 (2004).

[22] I. A. Hasnain and A. M. Donald, Phys. Rev. E **73**, 031901 (2006).

[23] T. A. Waigh, Rep. Prog. Phys. **68**, 685 (2005).

[24] J. C. Crocker, M. T. Valentine, E. R. Weeks, T. Gisler, P. D. Kaplan, A. G. Yodh, and D. A. Weitz, Phys. Rev. Lett. **85**, 888 (2000).

[25] A. J. Levine and T. C. Lubensky, Phys. Rev. Lett. **85**, 1774 (2000).

[26] M. J. Solomon and Q. Lu, Curr. Opin. Colloid Interface Sci. **6**, 430 (2001).

[27] I. Y. Wong, M. L. Gardel, D. R. Reichman, E. R. Weeks, M. T. Valentine, A. R. Bausch, and D. A. Weitz, Phys. Rev. Lett. **92**, 178101 (2004).

[28] A. Rahman, Phys. Rev. **136**, A405 (1964).

[29] W. K. Kegel and A. van Blaaderen, Science **287**, 290 (2000).

[30] E. R. Weeks, J. C. Crocker, A. C. Levitt, A. Schofield, and D. A. Weitz, Science **287**, 627 (2000).

[31] R. Tharmann, M. M. A. E. Claessens, and A. R. Bausch, Biophys. J. **90**, 2622 (2006).

[32] Y. Tseng and D. Wirtz, Biophys. J. **81**, 1643 (2001).

[33] P. Panorchan, D. Wirtz, and Y. Tseng, Phys. Rev. E **70**, 041906 (2004).

[34] D. D. Boos and C. Brownie, Stat. Sci. **19**, 571 (2004).

[35] A. Stuart and J. K. Ord, *Kendall's Advanced Theory of Statistics*, 6th ed. (Hodder Arnold, London, 1994), Vol. 1.

[36] D. Montiel, H. Cang, and H. Yang, J. Phys. Chem. B **110**, 19763 (2006).

[37] H. Flyvbjerg and H. G. Petersen, J. Chem. Phys. **91**, 461 (1989).

[38] R. Zwanzig and N. K. Ailawadi, Phys. Rev. **182**, 280 (1969).

[39] D. R. Bellhouse, Am. Stat. **55**, 352 (2001); software may be obtained from the American Statistician Software archive at http://lib.stat.cmu.edu/

[40] H. C. Öttinger, *Stochastic Processes in Polymeric Fluids: Tools and Examples for Developing Simulation Algorithms* (Springer-Verlag, New York, 1996).

[41] J. C. Love, D. B. Wolfe, H. O. Jacobs, and G. M. Whitesides, Langmuir **17**, 6005 (2001).

[42] D. Dendukuri, D. C. Pregibon, J. Collins, T. A. Hatton, and P. S. Doyle, Nat. Mater. **5**, 365369 (2006).

[43] T. Savin and P. S. Doyle, Phys. Rev. E **71**, 041106 (2005).

[44] T. Savin and P. S. Doyle, Biophys. J. **88**, 623 (2005).

[45] See EPAPS Document No. E-PLEEE8-75-142705 for a summary of the main notations used in this paper. For more information on EPAPS, see http://www.aip.org/pubservs/epaps.html.